AGU PUBLICATIONS

JGR

Journal of Geophysical Research: Space Physics

RESEARCH ARTICLE

10.1002/2017JA024513

Key Points:

- We investigate the evolution of lower band and upper band whistler waves excited by anisotropic hot electrons with 1-D PIC simulation
- We find that the amplitude of upper band waves tends to increase with the increase of the wave normal angle or the anisotropy of hot electrons
- The amplitude ratio is positively correlated with the wave normal angle but is anticorrelated with the anisotropy of hot electrons

Correspondence to:
X. Gao,
gaoxl@mail.ustc.edu.cn

Citation:
Chen, H., Gao, X., Lu, Q., Ke, Y., & Wang, S. (2017). Lower band cascade of whistler waves excited by anisotropic hot electrons: One-dimensional PIC simulations. *Journal of Geophysical Research: Space Physics*, *122*, 10,448–10,457. https://doi.org/10.1002/2017JA024513

Received 25 JUN 2017
Accepted 10 OCT 2017
Accepted article online 13 OCT 2017
Published online 30 OCT 2017

Lower Band Cascade of Whistler Waves Excited by Anisotropic Hot Electrons: One-Dimensional PIC Simulations

Huayue Chen[1,2,3], Xinliang Gao[1,2,3], Quanming Lu[1,2], Yangguang Ke[1,2], and Shui Wang[1,2]

[1]CAS Key Laboratory of Geospace Environment, Department of Geophysics and Planetary Science, University of Science and Technology of China, Hefei, China, [2]Collaborative Innovation Center of Astronautical Science and Technology, Harbin, China, [3]State Key Laboratory of Space Weather, Chinese Academy of Sciences, Beijing, China

Abstract Based on Time History of Events and Macroscale Interactions during Substorms waveform data, Gao, Lu, et al. (2016) have reported two special multiband chorus events, where upper band waves are located at harmonics of lower band waves. And they proposed a new generation mechanism to explain this multiband chorus wave, named as lower band cascade. With a 1-D particle-in-cell (PIC) simulation model, we have investigated the lower band cascade of whistler waves excited by anisotropic hot electrons. During each simulation, lower band whistler mode waves are firstly excited by the anisotropy of hot electrons. Later, upper band harmonic waves are generated through the nonlinear coupling between the electromagnetic and electrostatic components of lower band waves, which supports the scenario of lower band cascade. Moreover, the peak wave number (or frequency) of lower band waves will continuously drift to smaller values due to the decline of the anisotropy of hot electrons. While the peak wave number of upper band harmonic waves will be kept nearly unchanged, but their amplitude continues to decrease after their saturation. We further find that the magnetic amplitude of upper band harmonic waves tends to increase with the increase of the wave normal angle of lower band waves or the anisotropy of hot electrons. Besides, the amplitude ratio between upper band and lower band waves is positively correlated with the wave normal angle of lower band waves but is anticorrelated with the anisotropy of hot electrons. Our study has provided a more comprehensive understanding of the lower band cascade of whistler waves.

1. Introduction

Whistler mode chorus wave is one of intense plasma waves in the inner magnetosphere that occurs naturally near the magnetic equator during geoactive periods (Burtis & Helliwell, 1969; Gao, Mourenas, et al., 2016; Li et al., 2009; Santolík et al., 2005; Tsurutani & Smith, 1974). Chorus waves are typically detected within the frequency range of 0.1 to $0.8f_{ce}$, where f_{ce} is the equatorial electron gyrofrequency (Meredith et al., 2001; Santolík et al., 2003). Around $0.5f_{ce}$, there is usually a power gap in the spectrogram, which divides chorus waves into two separate bands: lower band (0.1–$0.5f_{ce}$) and upper band (0.5–$0.8f_{ce}$) (Koons & Roeder, 1990; Tsurutani & Smith, 1974). Whistler mode chorus waves in the inner magnetosphere can exhibit three kinds of time-frequency spectrogram, such as rising tones, falling tones, and hiss-like emissions (Gao et al., 2014a; Li et al., 2012; Santolík et al., 2003). Based on statistical results from Time History of Events and Macroscale Interactions during Substorms (THEMIS) satellites, chorus waves are observed to vary over a large range of the magnetic amplitude (~10 pT to ~1 nT), but they tend to have larger amplitudes during stronger geomagnetic activity (Li, Bortnik, et al., 2011). For lower band chorus waves, rising tones are mainly field aligned with the wave normal angle typically smaller than 30°, while falling tones are typically very oblique (Li, Thorne, et al., 2011). Whistler mode chorus waves are very significant in regulating electron populations in the Van Allen radiation belt due to their dual role in both loss and acceleration of radiation belt energetic electrons (Chen et al., 2007; Thorne et al., 2005). Chorus waves can not only efficiently scatter lower energy (0.1–30 keV) electrons into the loss cone, resulting in enhanced diffuse auroral precipitation into the Earth's atmosphere (Ni et al., 2011; Nishimura et al., 2013; Thorne et al., 2010), but also rapidly accelerate seed electrons (approximately hundreds of keV) up to relativistic energies (approximately MeV), refilling the outer Van Allen radiation belt during geomagnetic storms (Mourenas et al., 2014; Reeves et al., 2013; Summers et al., 1998; Thorne et al., 2013).

It has long been accepted that hot electrons (approximately tens of keV) with a sufficient temperature anisotropy $T_\perp > T_{||}$ ("$\perp$" and "||" denote perpendicular and parallel to the background magnetic field, respectively) can provide free energy to excite whistler mode waves (Gary et al., 2000; Helliwell, 1967; Kennel & Petschek, 1966; Li et al., 2009; Lu et al., 2004). However, the generation of whistler mode chorus waves in the Earth's magnetosphere still remains an open question. Although not yet fully understood, the generation of rising-tone chorus waves is now widely believed to involve both linear and nonlinear wave-particle interactions (Cully et al., 2011; Gao et al., 2014a; Hikishima et al., 2009; Katoh & Omura, 2007; Omura et al., 2008). With one-dimensional (1-D) particle-in-cell (PIC) simulations, many previous works have successfully reproduced parallel propagating rising-tone chorus waves (Hikishima et al., 2009; Katoh & Omura, 2007; Omura et al., 2008). Another mysterious property of whistler mode chorus waves in the magnetosphere is the power gap around $0.5f_{ce}$, which can separate upper band chorus from lower band chorus. Up to now, there have been several possible mechanisms proposed to explain this phenomenon (Fu et al., 2014; Omura et al., 2009). Omura et al. (2009) pointed out that the upper band chorus wave is just the extension of the lower band chorus wave but experiences a strong damping at about $0.5f_{ce}$ due to the inhomogeneity of the background magnetic field, while Fu et al. (2014) indicated that this gap is just a natural consequence of two anisotropic electron populations.

Recently, with THEMIS waveform data, Gao, Lu, et al. (2016) have reported two special multiband chorus events, where the upper band chorus wave is the second harmonic of the lower band chorus wave. Then, they proposed a new mechanism to explain this multiband chorus wave, named as lower band cascade, and further suggested that this could be a potential generation mechanism of upper band chorus waves. In this scenario, the upper band chorus wave is generated due to the nonlinear coupling between the electrostatic and electromagnetic components of the lower band chorus wave. With a 1-D PIC simulation model, Gao, Ke, et al. (2017) successfully reproduced multiband chorus waves and further confirmed the lower band cascade mechanism. In their simulations, the lower band chorus wave is simplified as a monochromatic whistler mode wave, which is injected in the system at the very beginning.

In this paper, with a 1-D PIC simulation model, we further investigate the lower band cascade of whistler waves excited by anisotropic hot electrons. In our simulations, the pump whistler mode waves are generated self-consistently by anisotropic hot electrons instead of the artificial injection, which also turn into a more realistic whistler mode spectrum. Moreover, we also study the time evolution of both lower band and upper band waves, how the amplitude of upper band harmonic waves and their amplitude ratio correlate with the wave normal angle (WNA)/anisotropy of hot electrons. The remainder of this paper is organized as follows. Section 2 describes the 1-D PIC simulation model and our initial setup. The simulation results are illustrated in section 3. At last, we summarize the principle results and give some discussions in section 4.

2. One-Dimensional PIC Simulation Model

The PIC simulation model has been widely applied in various researches on space physics (Gao, Ke, et al., 2017; Lu et al., 2004, 2010). The 1-D PIC simulation model with periodic boundary conditions allows spatial variations only in the x direction, meaning that the wave vector will be fixed along the x axis, but includes three-dimensional electromagnetic fields and velocities. The uniform background magnetic field $\mathbf{B_0} = B_0(\cos\theta\hat{\mathbf{x}} + \sin\theta\hat{\mathbf{z}})$ is lying in the (x, z) plane, where θ is the angle between the x axis and $\mathbf{B_0}$. The electromagnetic fields are defined on grids and calculated by integrating Maxwell equations with explicit "Leapfrog" algorithm (Birdsall & Langdon, 1991), while the full dynamics of particles can be obtained by solving the relativistic motion equation. In our simulations, there are three kinds of particles, such as protons, cold, and hot electrons. Note that protons are assumed to be an immobile neutralizing component since the frequencies of the investigated whistler mode waves are much larger than the ion cyclotron frequency.

In this simulation model, the time and space are normalized by the inverse of the electron gyrofrequency Ω_e^{-1} and the electron inertial length c/Ω_{pe} (c and Ω_{pe} denote the light speed and plasma frequency, respectively). The number of grid cells in the simulation box is $n_x = 2,400$ with its size as $\Delta x = 0.34V_{Ae}/\Omega_e$ (where $V_{Ae} = B_0/\sqrt{\mu_0 n_0 m_e}$, n_0 is the plasma density), and the total simulation time is about $800\Omega_e^{-1}$ with the time step as $\Delta t = 0.025\Omega_e^{-1}$. Here we set the ratio of the plasma frequency to electron gyrofrequency as $\Omega_{pe}/\Omega_e = 4$, which is a typical value at $L \approx 6$ ($L = r/R_E$, r is the distance to the Earth at the magnetic equator and R_E is

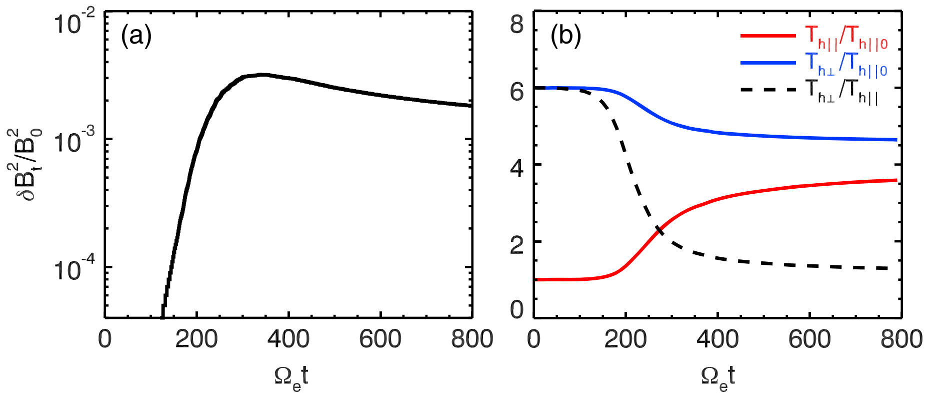

Figure 1. The time evolution of (a) transverse fluctuating magnetic fields $\delta B_t^2/B_0^2$ and (b) the parallel temperature $T_{h\,||}/T_{h\,||\,0}$ (red), perpendicular temperature $T_{h\perp}/T_{h\,||\,0}$ (blue), and anisotropy $T_{h\perp}/T_{h\,||}$ (black) of hot electrons, respectively.

the radius of the Earth), where the ambient magnetic field and plasma density are assumed to be B_0 = 150 nT and n_0 = 3.5 cm^{-3} (Gao et al., 2014b; Li et al., 2009). The mass ratio of proton to electron is set as 1836. For cold electrons, they satisfy the Maxwellian distribution with the thermal velocity as $v_c = 0.01 V_{Ae}$, that is, $\beta_{c\,||} = 9.2 \times 10^{-5}$, whose number density is chosen as 0.92 n_0, while hot electrons will satisfy a bi-Maxwellian distribution with their density as 0.08 n_0. Here protons have the same temperature as cold electrons, which means that their thermal velocity is ~2.3 × 10^{-4}V_{Ae}. If there is no any other explicit statements, the anisotropy of hot electrons is chosen as $T_{h\perp 0}/T_{h\,||\,0}$= 6 with their parallel thermal velocity as $v_{h\,||} = 1.0 V_{Ae}$, that is, $\beta_{h\,||} = 0.08$, and the WNA of excited whistler mode waves is fixed to $\theta = 30^\circ$. This plasma model has also been used in previous works (Gao et al., 2014a; Katoh & Omura, 2006, 2007). In order to efficiently reduce the noise level in the simulation system, we uniformly set average 5,000 macroparticles in every cell for each species.

3. Simulation Result

Figure 1 shows the time history of (a) transverse fluctuating magnetic fields $\delta B_t^2/B_0^2$ and (b) the parallel temperature $T_{h\,||}/T_{h\,||\,0}$ (red), perpendicular temperature $T_{h\perp}/T_{h\,||\,0}$ (blue), and anisotropy $T_{h\perp}/T_{h\,||}$ (black) of hot electrons, respectively. The transverse fluctuating magnetic field is given by $\delta B_t^2 = \delta B_y^2 + \delta B_z^2$. Based on the linear theory, the anisotropic hot electrons will be unstable to excite whistler mode waves. Just as shown in Figure 1a, whistler mode waves begin to grow from the background noise level around 100 Ω_e^{-1}, and saturate at about 300 Ω_e^{-1} with the intensity of fluctuating magnetic fields reaching up to $\delta B_t^2/B_0^2 \approx 3 \times 10^{-3}$. During linear growth of whistler mode waves, the perpendicular temperature of hot electrons rapidly decreases, while their parallel temperature gains a fast increase, leading to the reduction of the anisotropy $T_{h\perp}/T_{h\,||}$ from 6 to ~1.5 (Figure 1b).

Figure 2 displays the evolution of excited whistler mode waves, including the *k-t* spectrogram of (a) transverse fluctuating magnetic fields $\delta B_t/B_0$ and (b) fluctuating electric fields δE_x along the wave vector, and (c) time profiles of magnetic amplitudes of lower band whistler mode waves ($\delta B_{LW}/B_0$) and upper band harmonic waves ($\delta B_{HW}/B_0$), and their amplitude ratio ($\delta B_{HW}/\delta B_{LW}$), respectively. The black dashed lines in Figures 2a and 2b mark the wave number (~1.16$(V_{Ae}/\Omega_e)^{-1}$) at 0.5 Ω_e, which is estimated from the linear theory by using WHAMP model (https://github.com/irfu/whamp) (Rönnmark, 1982). As shown in Figure 2a, there is a clear power minimum around 0.5 Ω_e, which divides the whistler mode spectrum into lower band waves (LW) and upper band harmonic waves (HW). The lower band waves are firstly excited at about 100 Ω_e^{-1} from anisotropic hot electrons, whose peak wave number with the dominant magnetic power is at ~0.66$(V_{Ae}/\Omega_e)^{-1}$. However, during their subsequent growth, it is interesting to find that the peak wave number of lower band waves continuously decreases before 300Ω_e^{-1}, which was also reported by previous works (Lu et al., 2004; Sydora et al., 2007). This is just due to the fast decline of the anisotropy of hot electrons, which can be

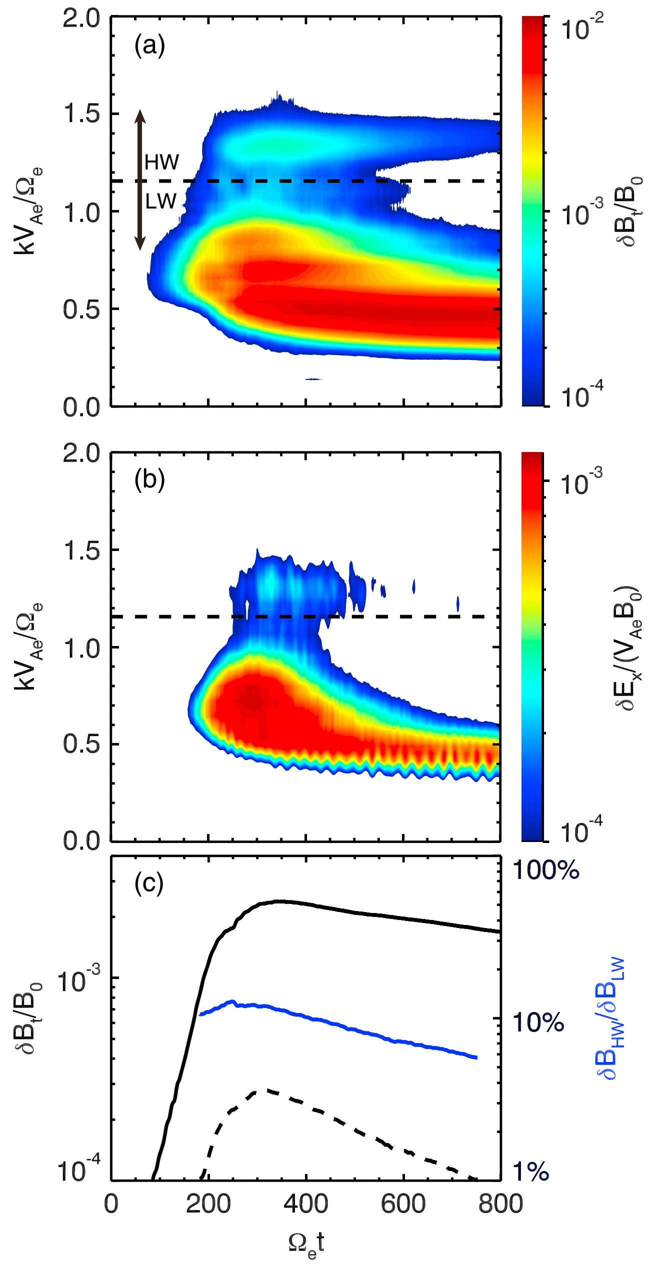

Figure 2. The *k*-*t* spectrogram of (a) transverse fluctuating magnetic fields $\delta B_t/B_0$ and (b) fluctuating electric fields δE_x along the wave vector; (c) time profiles of magnetic amplitudes of lower band whistler mode waves $\delta B_{LW}/B_0$ (black solid line) and upper band harmonic waves $\delta B_{HW}/B_0$ (black dashed line), and their amplitude ratio $\delta B_{HW}/\delta B_{LW}$ (blue line). In Figures 2a and 2b, the lower band waves (LW) and upper band harmonic waves (HW) are separated by the wave number at 0.5 Ω_e (black dashed lines) based on the linear theory.

further supported by the linear growth rate shown in Figure 4. For upper band waves, they begin to appear in the system at about 200 Ω_e^{-1} with the peak wave number as ~1.3 $(V_{Ae}/\Omega_e)^{-1}$, which is nearly twice that of lower band waves. Unlike lower band waves, the peak wave number of upper band harmonic waves nearly keeps constant after their generation, but upper band waves experience an obvious decline in the amplitude till the end of the simulation. Due to the finite wave normal angle of excited whistler mode waves, there are significant fluctuating electric fields along their wave vector as shown in Figure 2b, which are very important in the scenario of lower band cascade.

The magnetic amplitude for each band in Figure 2c is given by integrating the magnetic spectral density over three adjacent bins around the peak wave number at each time. Note that their amplitude ratio $\delta B_{HW}/\delta B_{LW}$ is plotted only when the amplitude of upper band harmonic waves is larger than 1.0×10^{-4}. The amplitude of lower band waves increases from ~100 Ω_e^{-1} and saturates at ~340 Ω_e^{-1} with $\delta B_{LW}/B_0 \approx 2.4 \times 10^{-3}$, while the amplitude of upper band harmonic waves starts to increase at a later time ~200 Ω_e^{-1} and saturates at ~320 Ω_e^{-1} with $\delta B_{HW}/B_0 \approx 2.8 \times 10^{-4}$. In Figure 2c, the amplitude ratio is found to be quite variable during the simulation, ranging from 6% to 13%, which is also consistent with observed values (~10^{-2} to ~10^{-1}) reported in Gao, Lu, et al. (2016).

To clearly exhibit the evolution of both lower band and upper band whistler mode waves, we plot the spectra of transverse fluctuating magnetic fields $\delta B_t/B_0$ at three selected time points in Figure 3: (a) $\Omega_e t$= 180, (b) $\Omega_e t$= 340, and (c) $\Omega_e t$= 600. The blue and red dashed lines denote the peak wave number for lower band and upper band waves, respectively. At $\Omega_e t$= 180, there only exist lower band whistler mode waves with the peak wave number as ~0.66 $(V_{Ae}/\Omega_e)^{-1}$ in the system (Figure 3a), which are still in the linear growth stage. When lower band waves saturate at about $\Omega_e t$= 340 (Figure 3b), their peak wave number has drifted to a smaller value of ~0.53 $(V_{Ae}/\Omega_e)^{-1}$. Meanwhile, upper band waves are also observed with a considerable amplitude, peaking at ~1.3 $(V_{Ae}/\Omega_e)^{-1}$, which is about 2.5 times that of lower band waves during this period. At $\Omega_e t$= 600, the peak wave number of lower band waves drifts to an even smaller value (~0.49 $(V_{Ae}/\Omega_e)^{-1}$), but their peak amplitude nearly keeps unchanged. However, upper band harmonic waves are significantly damped, but their peak wave number just keeps constant (Figure 3c). Therefore, at this time, the peak wave number of upper band waves now becomes 2.7 times that of lower band waves, which is far away from the harmonic of lower band waves.

The evolution of both lower band and upper band waves is further studied in Figure 4, which displays dispersion relations and linear growth rates of whistler mode waves for (a, b) $\Omega_e t$= 200–300 and (c, d) $\Omega_e t$= 300–400, respectively. The black line in Figure 4a or 4c is the dispersion relation of whistler mode waves obtained from the linear theory by using plasma parameters at the middle time of each interval. The linear growth rates in Figures 4b and 4d are calculated in the same way. And some necessary parameter values for linear theory calculations are listed in Table 1. We also mark the dominant wave mode with the maximum magnetic power by using white and red stars for lower band and upper band waves, respectively. During $\Omega_e t$= 200–300, the dominant wave mode for lower band waves is located at (~0.65 $(V_{Ae}/\Omega_e)^{-1}$, ~0.27 Ω_e) (Figure 4c), which is consistent with the most unstable mode given by the linear growth rate (Figure 4b). This indicates that lower band whistler mode waves should be linearly generated by the anisotropy of hot electrons, while the

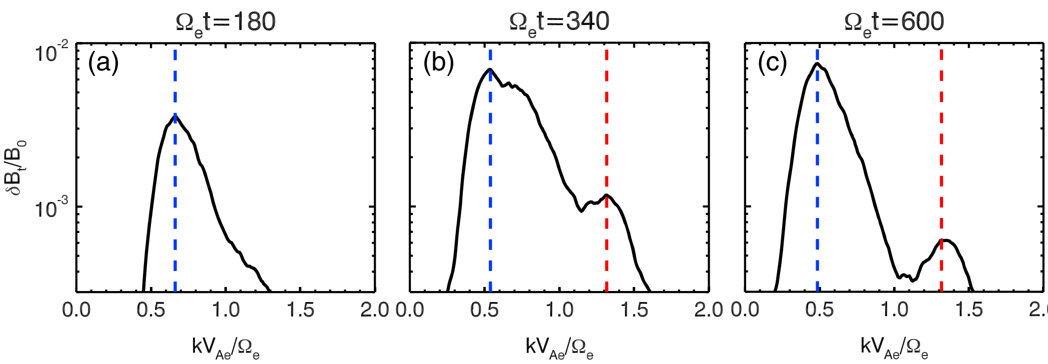

Figure 3. The spectra of transverse fluctuating magnetic fields $\delta B_t/B_0$ as a function of wave number at (a) $\Omega_e t$= 180, (b) $\Omega_e t$= 340, and (c) $\Omega_e t$= 600, respectively. The peak wave number for lower band and upper band waves are denoted by blue and red dashed lines, respectively.

dominant wave mode for upper band waves is located at (~1.30 $(V_{Ae}/\Omega_e)^{-1}$, ~0.56 Ω_e), which is just two times of that for lower band waves, that is, the second harmonic of lower band waves. However, the linear growth rate of upper band harmonic waves is almost zero, indicating that they cannot directly extract free energy from hot electrons, which indirectly supports that upper band waves should be excited through some nonlinear process, such as lower band cascade. As the time increases, the dominant wave mode of lower band waves has drifted to (~0.52 $(V_{Ae}/\Omega_e)^{-1}$, ~0.18 Ω_e) in Figure 4c, which is still consistent with the most unstable mode given by the linear growth rate in Figure 4d. This suggests that the frequency drift of lower

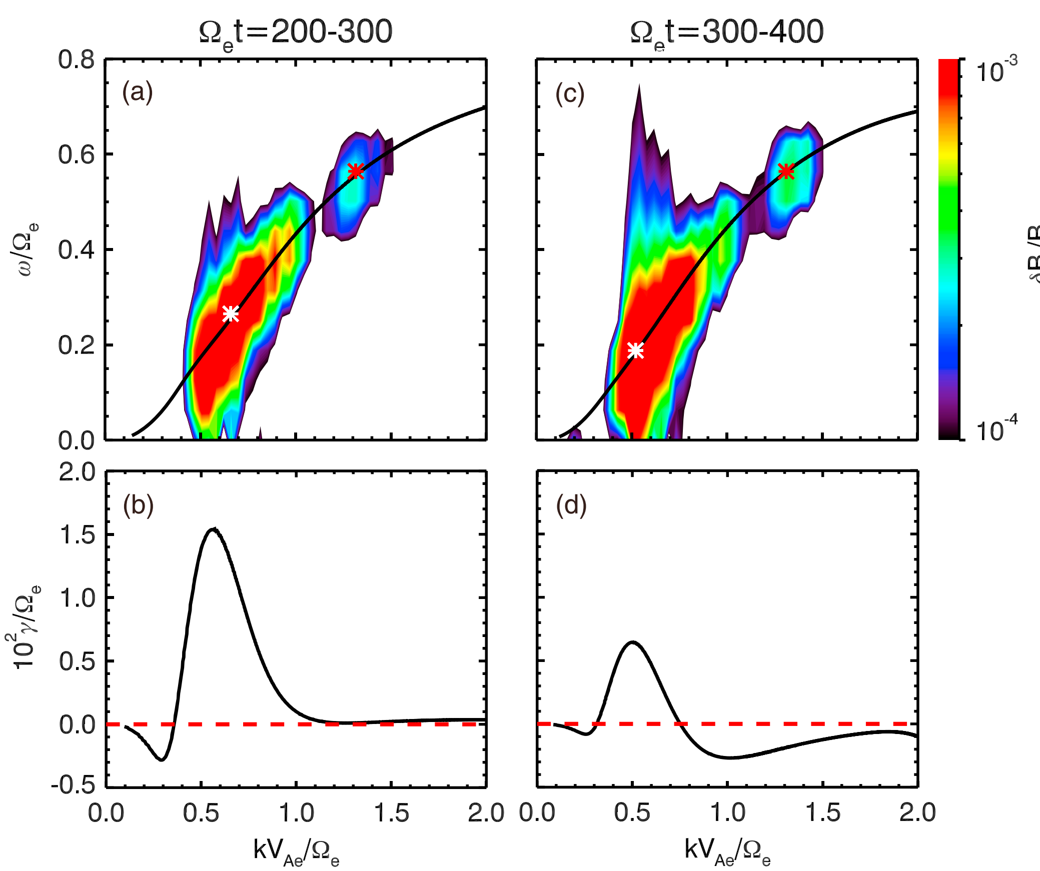

Figure 4. The dispersion relations of whistler mode waves obtained from two-dimensional Fourier transform of $\delta B_t/B_0$ and linear growth rates during: (a, b) $\Omega_e t$= 200–300 and (c, d) $\Omega_e t$= 300–400, respectively. In Figures 4a and 4c, the dominant wave modes are denoted by white and red stars for lower band and upper band waves, respectively.

Table 1
The Plasma Parameters for Linear Theory Calculations

Parameter	Value[a]	Value[b]
$v_{h\,||}/V_{Ae}$	1.41	1.69
$T_{h\perp}/T_{h\,||}$	2.71	1.70
$v_{c\,||}/V_{Ae}$	0.036	0.073
$T_{c\perp}/T_{c\,||}$	1.30	0.63

[a]Selected time $\Omega_e t = 250$. [b]Selected time $\Omega_e t = 350$

band waves should be controlled by a quasi-linear process, which is related to the decline of the anisotropy of hot electrons. For upper band waves, whose dominant wave mode just keeps unchanged, their growth rates are always negative (Figure 4d), meaning that they are damped in this system. This is quite consistent with the continuous decrease of the amplitude of upper band harmonic waves after ~300 Ω_e^{-1} shown in Figure 2.

We also calculate the bicoherence index (bc) to confirm the lower band cascade mechanism. Figure 5 shows the bicoherence index between the electromagnetic (δE_y) and electrostatic (δE_x) components of whistler mode waves for $\Omega_e t$= 300–350, when upper band harmonic waves reach the saturation. The bicoherence index is a widely used method to quantify the resonant condition among three waves (Gao, Lu, et al., 2016; Gao et al., 2014; Gao, Ke, et al., 2017; Gao, Lu, & Wang, 2017; Nariyuki & Hada, 2006; Nariyuki et al., 2009; van Milligen et al., 1995), which is given by $\left|\left\langle \delta E_x(k_{Ex})\delta E_y(k_{Ey})\delta E_y^*(k_{\mathrm{HW}})\right\rangle\right|^2/\left\langle\left|\delta E_x(k_{Ex})\delta E_y(k_{Ey})\right|^2\right\rangle\left\langle\left|\delta E_y^*(k_{\mathrm{HW}})\right|^2\right\rangle$ (where $k_{\mathrm{HW}} = k_{Ex} + k_{Ey}$, k_{Ey} and k_{Ex} are wave numbers of the electromagnetic (δE_y) and electrostatic (δE_x) components of lower band whistler mode waves, respectively, and the bracket $\langle\ldots\rangle$ denotes an average over a 50 Ω_e^{-1} time interval) in this study. The black dashed line in this panel marks the peak wave number of upper band waves, that is, $k_{Ex} + k_{Ey} = 1.30(V_{Ae}/\Omega_e)^{-1}$, where is also the high-bc region. The largest bc marked by a gray arrow is located at $k_{Ex}V_{Ae}/\Omega_e \approx 0.65$, $k_{Ey}V_{Ae}/\Omega_e \approx 0.65$, and $k_{\mathrm{HW}}V_{Ae}/\Omega_e \approx 1.30$ with bc = 0.72, meaning that there is strong coupling process among the electromagnetic (δE_y) and electrostatic (δE_x) components of lower band waves and the electromagnetic component (δE_y) of upper band waves. This is consistent with the scenario of lower band cascade (Gao, Lu, et al., 2016; Gao, Ke, et al., 2017).

The dependences of the magnetic amplitude of upper band harmonic waves on the wave normal angle of lower band whistler mode waves and the anisotropy of hot electrons are also studied. Figures 6a–6c exhibit the *k-t* spectrogram of $\delta B_t/B_0$ for cases of (a) $\theta = 10^\circ$ and $T_{h\perp 0}/T_{h\,||\,0}$= 4, (b) $\theta = 30^\circ$ and $T_{h\perp 0}/T_{h\,||\,0}$= 4, and (c) $\theta = 30^\circ$ and $T_{h\perp 0}/T_{h\,||\,0} = 8$, respectively. The black dashed lines just mark the wave number at the frequency 0.5 Ω_e based on the dispersion relation of the linear theory. And Figure 6d gives the spectrum of $\delta B_t/B_0$ as a function of the wave number for cases (a) and (c) at the time when lower band waves reach their saturation. As shown in Figures 6a and 6b, upper band harmonic waves are produced in the system for both cases. Although the magnetic amplitude of lower band waves is smaller in case (b), the generated upper band waves have a larger magnetic amplitude, which should be resulted from the larger electrostatic component of lower band waves for $\theta = 30^\circ$. To further show the importance of the electrostatic component, we also performed another run with $\theta = 30^\circ$ and $T_{h\perp 0}/T_{h\,||\,0} = 8$. As shown in Figure 6d, lower band whistler mode waves have the nearly same magnetic amplitude in cases (a) and (c), while the electrostatic component of lower band waves is much larger for the more oblique case $\theta = 30^\circ$ (not shown here). Therefore, upper band waves are generated through lower band cascade with a much larger amplitude for the case of $\theta = 30^\circ$. This is also consistent with observations by Gao, Lu, et al. (2016), where they found that the amplitude threshold of lower band cascade for lower band waves with larger WNAs is smaller. Figure 7 displays the *k-t* spectrogram of $\delta B_t/B_0$ for three cases of (a) A = 3, (b) A = 4, and (c) $A = 6$, respectively, where $A \equiv T_{h\perp 0}/T_{h\,||\,0}$. Here the wave normal angle is fixed at $\theta = 30^\circ$ for three cases. In all panels, the black dashed lines mark the wave number at 0.5 Ω_e based on the linear theory. For all cases, there are two-band whistler mode waves excited in the system with a power minimum around 0.5 Ω_e. Moreover, there is a clear trend that the magnetic amplitude of upper band waves increases as the increase of the anisotropy of hot electrons, which is mainly due to the enhanced lower band waves.

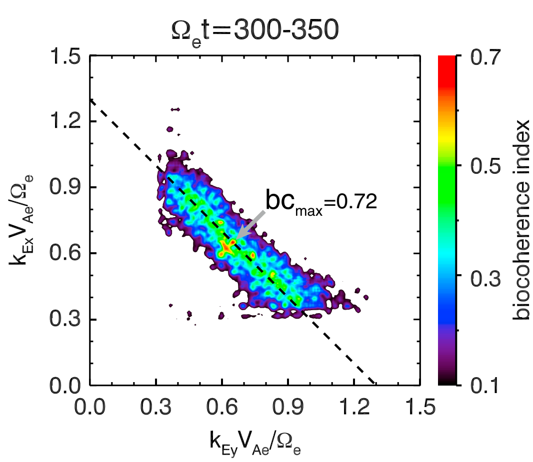

Figure 5. The bicoherence indices between electromagnetic (δE_y) and electrostatic (δE_x) components of whistler mode waves for $\Omega_e t$= 300–350. The black dashed line corresponds to $k_{Ex} + k_{Ey} = 1.30(V_{Ae}/\Omega_e)^{-1}$, while the gray arrow marks the maximum bc.

Figure 8 shows the amplitude ratio $\delta B_{\mathrm{HW}}/\delta B_{\mathrm{LW}}$ between upper band and lower band waves as a function of the wave normal angle θ for different

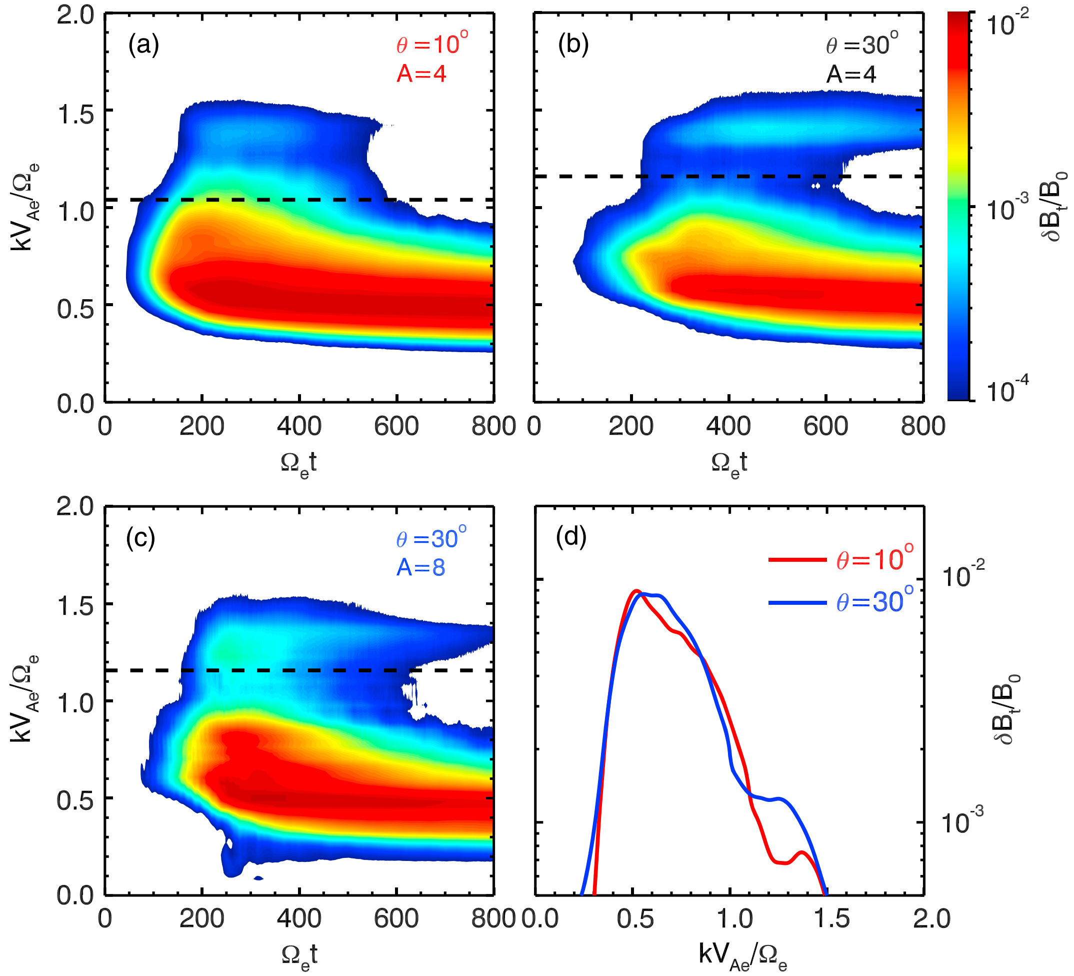

Figure 6. The *k-t* spectrogram of transverse fluctuating magnetic fields $\delta B_t/B_0$ obtained from the fast Fourier transform for the case (a) $\theta = 10^\circ$ and $T_{h\perp0}/T_{h\parallel0} = 4$, (b) $\theta = 30^\circ$ and $T_{h\perp0}/T_{h\parallel0} = 4$, and (c) $\theta = 30^\circ$ and $T_{h\perp0}/T_{h\parallel0} = 8$, respectively; (d) the spectrum of $\delta B_t/B_0$ as a function of the wave number for both Figures 6a and 6c at the time when lower band waves reach their saturation. The red and blue lines in Figure 6d represent Figures 6a and 6c, respectively.

anisotropies of hot electrons. Each symbol "*" denotes a simulation run, which is color coded by the anisotropy of hot electrons. Here the amplitude ratio is calculated at the saturation time of upper band waves. As shown in Figure 8, the amplitude ratio is found to vary over a large range of 5%–20%, and the observed amplitude ratios also fall in this range (Gao, Lu, et al., 2016). Clearly, the amplitude ratio is

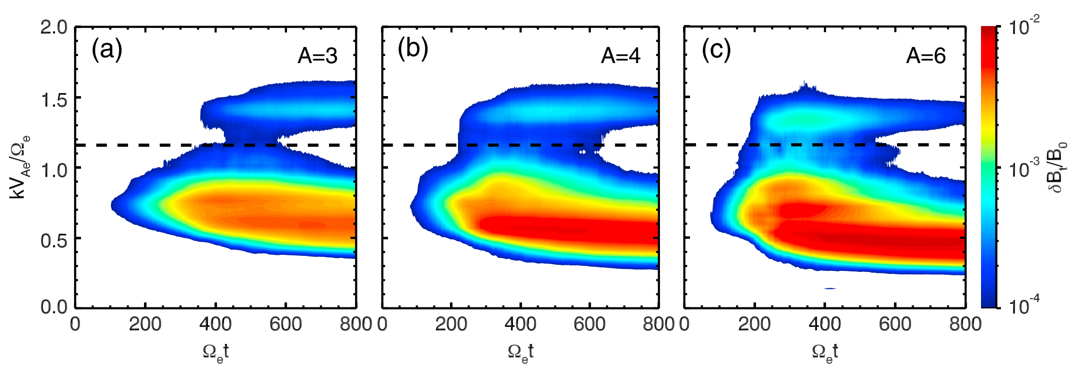

Figure 7. The *k-t* spectrogram of $\delta B_t/B_0$ for three cases of (a) $A = 3$, (b) $A = 4$, and (c) $A = 6$, respectively. Here the wave normal angle is fixed at θ= 30° for all cases and the black dashed lines mark the wave number at 0.5 Ω_e estimated from linear theory.

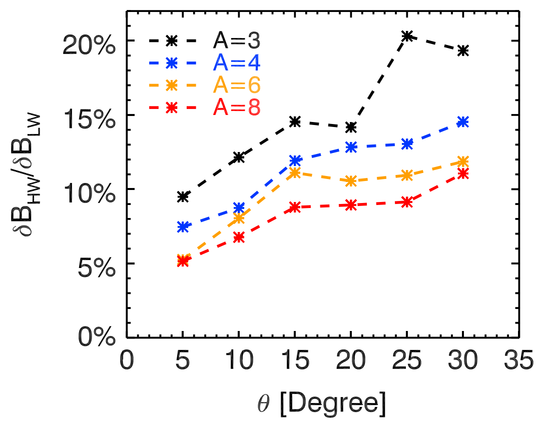

Figure 8. The amplitude ratio $\delta B_{\mathrm{HW}}/\delta B_{\mathrm{LW}}$ between upper band and lower band waves as a function of the wave normal angle θ for different anisotropies of hot electrons. Each symbol "*" denotes a simulation run, which is color coded by the anisotropy (A) of hot electrons.

positively correlated with the wave normal angle of lower band waves but is anticorrelated with the anisotropy of hot electrons. It is worth noting that the amplitude ratio is quite variable during each simulation run (Figure 2c), which is due to the evolution of both lower band and upper band waves. However, we still get the same trend of the amplitude ratio with the wave normal angle of lower band waves and the anisotropy of hot electrons, when the amplitude ratio is calculated at the saturation time of lower band waves.

4. Conclusions and Discussion

With a 1-D PIC simulation model, we have investigated the lower band cascade of whistler waves excited by anisotropic hot electrons. Lower band whistler mode waves are firstly excited due to the anisotropy of hot electrons, whose peak wave number and frequency are consistent with the most unstable mode given by the linear theory. Then, upper band harmonic waves are generated through the coupling between the electromagnetic and electrostatic components of lower band waves, which supports the scenario of lower band cascade. Moreover, the peak wave number (or frequency) of lower band waves will gradually drift to smaller values due to the decline of the anisotropy of hot electrons, while the peak wave number of upper band harmonic waves are kept unchanged, but their amplitude continuously decreases after the saturation. We further find that the magnetic amplitude of upper band harmonic waves tends to increase with the increase of the wave normal angle of lower band waves or the anisotropy of hot electrons. Besides, the amplitude ratio between upper band and lower band waves is positively correlated with the wave normal angle of lower band waves but is anticorrelated with the anisotropy of hot electrons.

Based on THEMIS waveform data, Gao, Lu, et al. (2016) have reported two special multiband chorus events, where the upper band chorus wave is the harmonic of the lower band chorus wave. Then, they proposed a new mechanism to explain this multiband chorus wave, named as lower band cascade, and further suggested that this could be a potential generation mechanism of upper band chorus waves. With a 1-D PIC simulation model, Gao, Ke, et al. (2017) successfully reproduced multiband chorus waves and confirmed the lower band cascade mechanism. In this study, we initialize the simulation model with anisotropic hot electrons instead of injecting a monochromatic pump whistler mode wave (Gao, Ke, et al., 2017), which is a more self-consistent initial setup. As a result, whistler mode waves generated in our simulations are more like those observed in the Earth's magnetosphere, whose spectrum typically haves a finite bandwidth.

Based on satellite observations, upper band chorus emissions usually have larger wave normal angles compared with lower band chorus waves (Li, Bortnik, et al., 2011). In Figures 6 and 8, lower band cascade is stronger (or easily to occur) for lower band waves with larger WNAs, which means that upper band waves tend to be excited with larger WNAs. Therefore, upper band waves may be observed typically with a larger WNA in the magnetosphere. Moreover, the power gap at $0.5f_{ce}$ will not be found if the frequencies of lower band waves are over $0.25f_{ce}$, which is also reported in Gao, Lu, et al. (2016) (Figure 5). However, Kurita et al. (2012) also reported several rising-tone chorus events without a power gap, which can be explained by the nonlinear wave growth theory of Omura et al. (2008).

More interestingly, the peak wave number (or frequency) of lower band waves will gradually drift to smaller values during the simulation, but the peak wave number of upper band harmonic waves is kept nearly constant (Figures 2 and 3). Therefore, their wave number ratio can become much larger than 2, meaning that upper band waves are no longer the second harmonic of lower band waves. This suggests that even though upper band chorus waves are not observed to be harmonics of lower band waves in the Earth's magnetosphere, they may still be generated through the lower band cascade. Besides, upper band waves continuously decay after their saturation (Figures 2 and 3), which is also predicted by the negative linear growth rate shown in Figure 4d. Since upper band waves have the larger wave number and frequency, they are more easily resonant with energetic electrons. Here for upper band waves, the resonant velocities for cyclotron and Landau resonances are about 0.39 V_{Ae} and 0.50 V_{Ae}, which indicates the cyclotron resonance is more important here. However, to fully understand interactions between upper band waves and electrons and quantify their contribution to energization of electrons still require a full study, which is beyond the scope of this paper. Note that these excited upper band waves through lower band cascade are driven modes, rather than normal modes in this plasma system, which means that upper band waves may not necessarily satisfy the dispersion relation of whistler mode waves.

Acknowledgments
This research was supported by the NSFC grants 41774151, 41604128, 41631071, 41331067, and 41474125, Youth Innovation Promotion Association of Chinese Academy of Sciences (2016395), Specialized Research Fund for State Key Laboratories, and Key Research Program of Frontier Sciences, CAS (QYZDJ-SSW-DQC010). The simulation data will be preserved on a long-term storage system and will be made available upon request to the corresponding author.

References

Birdsall, C. K., & Langdon, A. B. (1991). *Plasma physics via computer simulation*. Philadelphia, PA: IOP Publ. https://doi.org/10.1887/0750301171

Burtis, W. J., & Helliwell, R. A. (1969). Banded chorus a new type of VLF radiation observed in the magnetosphere by OGO 1 and OGO 3. *Journal of Geophysical Research*, *74*(11), 3002–3010. https://doi.org/10.1029/JA074i011p03002

Chen, Y., Reeves, G. D., & Friedel, R. H. W. (2007). The energization of relativistic electrons in the outer Van Allen radiation belt. *Nature Physics*, *3*(9), 614–617. https://doi.org/10.1038/nphys655

Cully, C. M., Angelopoulos, V., Auster, U., Bonnell, J., & Le Contel, O. (2011). Observational evidence of the generation mechanism for rising-tone chorus. *Geophysical Research Letters*, *38*, L01106. https://doi.org/10.1029/2010GL045793

Fu, X. R., Cowee, M. M., Friedel, R. H., Funsten, H. O., Gary, S. P., Hospodarsky, G. B., … Winske, D. (2014). Whistler anisotropy instabilities as the source of banded chorus: Van Allen Probes observations and particle-in-cell simulations. *Journal of Geophysical Research: Space Physics*, *119*, 8288–8298. https://doi.org/10.1002/2014JA020364

Gao, X., Li, W., Thorne, R. M., Bortnik, J., Angelopoulos, V., Lu, Q., … Wang, S. (2014b). Statistical results describing the bandwidth and coherence coefficient of whistler mode waves using THEMIS waveform data. *Journal of Geophysical Research: Space Physics*, *119*, 8992–9003. https://doi.org/10.1002/2014JA020158

Gao, X. L., Ke, Y. G., Lu, Q. M., Chen, L. J., & Wang, S. (2017). Generation of multiband chorus in the Earth's magnetosphere: 1-D PIC simulation. *Geophysical Research Letters*, *44*(2), 618–624. https://doi.org/10.1002/2016GL072251

Gao, X. L., Li, W., Thorne, R. M., Bortnik, J., Angelopoulos, V., Lu, Q. M., … Wang, S. (2014a). New evidence for generation mechanisms of discrete and hiss-like whistler mode waves. *Geophysical Research Letters*, *41*(14), 4805–4811. https://doi.org/10.1002/2014GL060707

Gao, X. L., Lu, Q. M., Bortnik, J., Li, W., Chen, L. J., & Wang, S. (2016). Generation of multiband chorus by lower band cascade in the Earth's magnetosphere. *Geophysical Research Letters*, *43*(6), 2343–2350. https://doi.org/10.1002/2016GL068313

Gao, X. L., Lu, Q. M., Li, X., Hao, Y. F., Tao, X., & Wang, S. (2014). Ion dynamics during the parametric instabilities of a left-hand polarized Alfven wave in a proton-electron-alpha plasma. *The Astrophysical Journal*, *780*(1), 56. https://doi.org/10.1088/0004-637X/780/1/56

Gao, X. L., Lu, Q. M., & Wang, S. (2017). First report of resonant interactions between whistler mode waves in the Earth's magnetosphere. *Geophysical Research Letters*, *44*(11), 5269–5275. https://doi.org/10.1002/2017GL073829

Gao, X. L., Mourenas, D., Li, W., Artemyev, A. V., Lu, Q. M., Tao, X., & Wang, S. (2016). Observational evidence of generation mechanisms for very oblique lower band chorus using THEMIS waveform data. *Journal of Geophysical Research: Space Physics*, *121*, 6732–6748. https://doi.org/10.1002/2016JA022915

Gary, S. P., Winske, D., & Hesse, M. (2000). Electron temperature anisotropy instabilities: Computer simulations. *Journal of Geophysical Research*, *105*(A5), 10,751–10,759. https://doi.org/10.1029/1999JA000322

Helliwell, R. A. (1967). A theory of discrete emissions from the magnetosphere. *Journal of Geophysical Research*, *72*(19), 4773–4790. https://doi.org/10.1029/JZ072i019p04773

Hikishima, M., Yagitani, S., Omura, Y., & Nagano, I. (2009). Full particle simulation of whistler-mode rising chorus emissions in the magnetosphere. *Journal of Geophysical Research*, *114*, A01203. https://doi.org/10.1029/2008JA013625

Katoh, Y., & Omura, Y. (2006). A study of generation mechanism of VLF triggered emission by self-consistent particle code. *Journal of Geophysical Research*, *111*, A12207. https://doi.org/10.1029/2006JA011704

Katoh, Y., & Omura, Y. (2007). Computer simulation of chorus wave generation in the Earth's inner magnetosphere. *Geophysical Research Letters*, *34*, L03102. https://doi.org/10.1029/2006GL028594

Kennel, C. F., & Petschek, H. E. (1966). Limit on stably trapped particle fluxes. *Journal of Geophysical Research*, *71*(1), 1–28. https://doi.org/10.1029/JZ071i001p00001

Koons, H. C., & Roeder, J. L. (1990). A survey of equatorial magnetospheric wave activity between 5 and 8 R_E. *Planetary and Space Science*, *38*(10), 1335–1341. https://doi.org/10.1016/0032-0633(90)90136-E

Kurita, S., Katoh, Y., Omura, Y., Angelopoulos, V., Cully, C. M., Le Contel, O., & Misawa, H. (2012). THEMIS observation of chorus elements without a gap at half the gyrofrequency. *Journal of Geophysical Research*, *117*, A11223. https://doi.org/10.1029/2012JA018076

Li, W., Bortnik, J., Thorne, R. M., & Angelopoulos, V. (2011). Global distribution of wave amplitudes and wave normal angles of chorus waves using THEMIS wave observations. *Journal of Geophysical Research*, *116*, A12205. https://doi.org/10.1029/2011JA017035

Li, W., Thorne, R. M., Angelopoulos, V., Bonnell, J. W., McFadden, J. P., Carlson, C. W., … Auster, H. U. (2009). Evaluation of whistler-mode chorus intensification on the nightside during an injection event observed on the THEMIS spacecraft. *Journal of Geophysical Research*, *114*, A00C14. https://doi.org/10.1029/2008JA013554

Li, W., Thorne, R. M., Bortnik, J., Shprits, Y. Y., Nishimura, Y., Angelopoulos, V., … Bonnell, J. W. (2011). Typical properties of rising and falling tone chorus waves. *Geophysical Research Letters*, *38*, L14103. https://doi.org/10.1029/2011GL047925

Li, W., Thorne, R. M., Bortnik, J., Tao, X., & Angelopoulos, V. (2012). Characteristics of hiss-like and discrete whistler-mode emissions. *Geophysical Research Letters*, *39*, L18106. https://doi.org/10.1029/2012GL053206

Lu, Q. M., Wang, L. Q., Zhou, Y., & Wang, S. (2004). Electromagnetic instabilities excited by electron temperature anisotropy. *Chinese Physics Letters*, *21*(8), 1518–1521. https://doi.org/10.1088/0256-307X/21/8/029

Lu, Q. M., Zhou, L. H., & Wang, S. (2010). Particle-in-cell simulations of whistler waves excited by an electron kappa distribution in space plasma. *Journal of Geophysical Research*, *115*, A02213. https://doi.org/10.1029/2009JA014580

Meredith, N. P., Horne, R. B., & Anderson, R. R. (2001). Substorm dependence of chorus amplitudes: Implications for the acceleration of electrons to relativistic energies. *Journal of Geophysical Research*, *106*(A7), 13,165–13,178. https://doi.org/10.1029/2000JA900156

Mourenas, D., Artemyev, A., Agapitov, O., & Krasnoselskikh, V. (2014). Consequences of geomagnetic activity on energization and loss of radiation belt electrons by oblique chorus waves. *Journal of Geophysical Research: Space Physics*, *119*(4), 2775–2796. https://doi.org/10.1002/2013JA019674

Nariyuki, Y., & Hada, T. (2006). Remarks on nonlinear relation among phases and frequencies in modulational instabilities of parallel propagating Alfven waves. *Nonlinear Processes in Geophysics*, *13*(4), 425–441. https://doi.org/10.5194/npg-13-425-2006

Nariyuki, Y., Hada, T., & Tsubouchi, K. (2009). Parametric instabilities of circularly polarized Alfven waves in plasmas with beam protons. *Journal of Geophysical Research*, *114*, A07102. https://doi.org/10.1029/2009JA014178

Ni, B. B., Thorne, R. M., Shprits, Y. Y., Orlova, K. G., & Meredith, N. P. (2011). Chorus-driven resonant scattering of diffuse auroral electrons in nondipolar magnetic fields. *Journal of Geophysical Research*, *116*, A06225. https://doi.org/10.1029/2011JA016453

Nishimura, Y., Bortnik, J., Li, W., Thorne, R. M., Ni, B., Lyons, L. R., … Auster, U. (2013). Structures of dayside whistler-mode waves deduced from conjugate diffuse aurora. *Journal of Geophysical Research: Space Physics*, *118*(2), 664–673. https://doi.org/10.1029/2012JA018242

Omura, Y., Hikishima, M., Katoh, Y., Summers, D., & Yagitani, S. (2009). Nonlinear mechanisms of lower-band and upper-band VLF chorus emissions in the magnetosphere. *Journal of Geophysical Research*, *114*, A07217. https://doi.org/10.1029/2009JA014206

Omura, Y., Katoh, Y., & Summers, D. (2008). Theory and simulation of the generation of whistler-mode chorus. *Journal of Geophysical Research*, *113*, A04223. https://doi.org/10.1029/2007JA012622

Reeves, G. D., Spence, H. E., Henderson, M. G., Morley, S. K., Friedel, R. H. W., Funsten, H. O., … Niehof, J. T. (2013). Electron acceleration in the heart of the Van Allen radiation belts. *Science*, *341*(6149), 991–994. https://doi.org/10.1126/science.1237743

Rönnmark, K. (1982). WHAMP: Waves in homogeneous, anisotropic multicomponent plasmas (Rep. 179, pp. 1–60). Kiruna, Sweden: Kiruna Geophysical Institute.

Santolík, O., Gurnett, D. A., Pickett, J. S., Parrot, M., & Cornilleau-Wehirlin, N. (2005). Central position of the source region of storm-time chorus. *Planetary and Space Science*, *53*(1-3), 299–305. https://doi.org/10.1016/j.pss.2004.09.056

Santolík, O., Gurnett, D. A., Pickett, J. S., Parrot, M., & N. Cornilleau-Wehrlin (2003), Spatio-temporal structure of storm-time chorus, *Journal of Geophysical Research*, *108*(A7), 1278. https://doi.org/10.1029/2002JA009791

Summers, D., Thorne, R. M., & Xiao, F. (1998). Relativistic theory of wave-particle resonant diffusion with application to electron acceleration in the magnetosphere. *Journal of Geophysical Research*, *103*(A9), 20,487–20,500. https://doi.org/10.1029/98JA01740

Sydora, R. D., Sauer, K., & Silin, I. (2007). Coherent whistler waves and oscilliton formation: Kinetic simulations. *Geophysical Research Letters*, *34*, L22105. https://doi.org/10.1029/2007GL031839

Thorne, R. M., Li, W., Ni, B., Ma, Q., Bortnik, J., Chen, L., … Kanekal, S. G. (2013). Rapid local acceleration of relativistic radiation-belt electrons by magnetospheric chorus. *Nature*, *504*(7480), 411–414. https://doi.org/10.1038/nature12889

Thorne, R. M., Ni, B., Tao, X., Horne, R. B., & Meredith, N. P. (2010). Scattering by chorus waves as the dominant cause of diffuse auroral precipitation. *Nature*, *467*(7318), 943–946. https://doi.org/10.1038/nature09467

Thorne, R. M., O'Brien, T. P., Shprits, Y. Y., Summers, D., & Horne, R. B. (2005). Timescale for MeV electron microburst loss during geomagnetic storms. *Journal of Geophysical Research*, *110*, A09202. https://doi.org/10.1029/2004JA010882

Tsurutani, B. T., & Smith, E. J. (1974). Postmidnight chorus: A substorm phenomenon. *Journal of Geophysical Research*, *79*(1), 118–127. https://doi.org/10.1029/JA079i001p00118

van Milligen, B. P., Sanchez, E., Estrada, T., Hidalgo, C., Branas, B., Carreras, B., & Garcia, L. (1995). Wavelet bicoherence: A new turbulence analysis tool. *Physics of Plasmas*, *2*, 3017–3032. https://doi.org/10.1063/1.871199